J. Fluid Mech. (2006), *vol.* 562, *pp.* 73–82.
doi:10.1017/S0022112006001182 Printed in the United Kingdom

Spiral patterns of inertia–gravity waves in geophysical flows

By ÁLVARO VIÚDEZ

Institut de Ciènces del Mar, CSIC, Barcelona, Spain
aviudez@cmima.csic.es

(Received 17 December 2005 and in revised form 26 May 2006)

High-resolution three-dimensional numerical experiments show that initially balanced (void of waves) geophysical flows, static and inertially stable, generate spiral patterns of small-amplitude inertia–gravity waves (IGWs). The spiral wave patterns are due to the spontaneous generation of IGW packets emitted from fluid volumes (the IGW sources) experiencing large local changes of potential vorticity. The IGW packets spread away from the vortical flow and cause spiral wave patterns of the same sense of spiralling, cyclonic or anticyclonic, as the moving IGW sources. The spiral patterns are noticeable in the vertical velocity in deep layers, away from the large-amplitude balanced vertical velocity. The generation of the spiral wave patterns is illustrated through several examples, namely, the single ellipsoidal vortex (cyclone and anticyclone), the merging of two spherical vortices, the dipole, and the anticyclonic shear instability.

1. Introduction

Travelling spiral or helical waves have been a fertile topic of recent research, especially the waves in pressure-driven flow through axially rotating circular pipes (e.g. Smith & Bodonyi 1982; Toplosky & Akylas 1988; Barnes & Kerswell 2000). The interest in these waves is partly related to the flow stability since they might be a necessary phenomenon in the transition from laminar to turbulent flow (e.g. Wedin & Kerswell 2004). Geophysical fluids of the balanced f-plane mesoscale dynamics are also rotating, though their motion is baroclinic, stably stratified, inertially stable, and mostly horizontal (perpendicular to the gravity field). Many geophysical density fronts and jets are baroclinically unstable and experience a transition to the state of geostrophic turbulence (e.g. Molemaker, McWilliams & Yavneh 2005).

This paper shows, from high-resolution three-dimensional numerical simulations, that generation of spiral waves is also a robust phenomenon in balanced (initially void of inertia–gravity waves, IGWs) baroclinic geophysical flows that remain static and inertially stable. The vortical flow spontaneously generates, in regions of large potential vorticity (PV) advection, perturbations that propagate away from the vortical flow and towards regions where, owing to the small horizontal pressure gradients, inertial, polarized waves are possible.

The generation of spiral wave patterns is illustrated through several examples, differing in the initial distributions of the single ellipsoidal vortex: two interacting spherical vortices, the dipole, and the anticyclonic shear instability. Owing to the small magnitude of the vertical motion relative to the horizontal motion in balanced mesoscale geophysical flows, the spiral waves are noticeable in the vertical velocity

distributions, in horizontal layers below (or above) the vortical flow. The vortical flow continues to be largely in balance, however, in the sense that the horizontal motion remains several orders of magnitude larger than the horizontal velocity of the IGWs.

2. Numerical results

2.1. *Numerical model*

The three-dimensional baroclinic, geophysical (rotating and stably stratified), volume-preserving non-hydrostatic flow, under the Boussinesq approximation, is simulated using a triply periodic numerical model (Dritschel & Viúdez 2003) initialized using the PV initialization approach (Viúdez & Dritschel 2003). The PV is represented by contours lying on isopycnals. We use a 256^3 grid in a domain of vertical extent $L_z = 2\pi$ (which defines the unit of length) and horizontal extents $L_x = L_y = cL_z$, where $c \equiv 10$ is the ratio of the mean Brunt–Väisälä to the constant Coriolis frequency $c \equiv \epsilon^{-1} \equiv N/f$. We take the (mean) buoyancy period ($T_{\rm bp} \equiv 2\pi/N$) as the unit of time by setting $N \equiv 2\pi$. One inertial period ($T_{\rm ip} \equiv 2\pi/f$) equals $10\,T_{\rm bp}$. The time step $\delta t = 0.01$, and initialization time $t_I = 5\,T_{\rm ip}$. The initialization time is the minimum time required for the fluid to reach its initial perturbed state with minimal generation of IGWs.

The vertical displacement $\mathscr{D}$ of isopycnals with respect to the reference density configuration is $\mathscr{D}(\boldsymbol{x}, t) \equiv z - d(\boldsymbol{x}, t)$, where $d \equiv (\rho - \rho_0)/\varrho_z$ is the depth, or vertical location, that an isopycnal located at $\boldsymbol{x}$ at time t has in the reference density configuration defined by $\rho_0 + \varrho_z z$, where ρ is the mass density and $\rho_0 > 0$ and $\varrho_z < 0$ are given constants. Static instability occurs when $\mathscr{D}_z \equiv \partial\mathscr{D}/\partial z > 1$. The Rossby number $\mathscr{R} \equiv \zeta/f$, and the Froude number $\mathscr{F} \equiv \omega_h/\mathscr{N}$, where ω_h and ζ are the horizontal and vertical components of the relative vorticity $\boldsymbol{\omega}$, respectively, and $\mathscr{N}$ is the total Brunt–Väisälä frequency. The PV anomaly $\varpi \equiv \Pi - 1$, where $\Pi \equiv (\boldsymbol{\omega}/f + \boldsymbol{k})\cdot\nabla d$ is the dimensionless total PV.

2.2. *Ellipsoidal vortex*

A simple example of a vortical structure generating patterns of spiral IGWs is the anticyclone (figure 1*a*) here simulated as an ellipsoidal PV vortex with a ratio of horizontal major (A_x) to minor (A_y) axes length $A_x/A_y = 1.6$. In the middle layer ($z = 0$, grid index $i_z = 129$) the largest PV ellipse has $A_x = 1.6c$, $A_y = c$, and vertical axis $A_z = 1$. The minimum dimensionless PV anomaly $\varpi_{\rm min} = -0.95$ (details of the vortex PV configuration are given in Viúdez & Dritschel 2003). After the initialization period and in shallow layers the large scale (mesoscale) w has a quadrupolar pattern and remains largely in balance since the small-amplitude IGWs are unnoticeable at this depth (figure 1*b*). At mid layers the magnitude of the balanced w decreases and both the balanced and the spiral patterns of IGWs are observed (figure 1*b*). In deeper layers, away from the vortical flow, the spiral patterns of small-amplitude IGWs (as well as larger scale symmetric waves due to the numerical initialization) are clearly noticeable (figure 1*c*). The spiralling of the IGW patterns is anticyclonic, here meaning in the sense of rotation as one moves from the waves generated previously (old waves, thus located far away from the vortex) to the waves generated recently (new waves, thus located closer to the vortex). The mesoscale w is typically 10^2 times larger than the vertical velocity of the IGWs. The flow remains static and inertially stable reaching, between $t = 5\,T_{\rm ip}$ and $9\,T_{\rm ip}$, extreme values of $\mathscr{R}_{\rm min} = -0.90$, $\mathscr{F}_{\rm max} = 0.49$, and $\mathscr{D}_{z\rm max} = 0.32$, with time-averaged values $\langle\mathscr{R}_{\rm min}\rangle = -0.90$ (± 0.0004), $\langle\mathscr{F}_{\rm max}\rangle = 0.48$ (± 0.006), and $\langle\mathscr{D}_{z\rm max}\rangle = 0.32$ (± 0.0008). The horizontal speed u_h is of

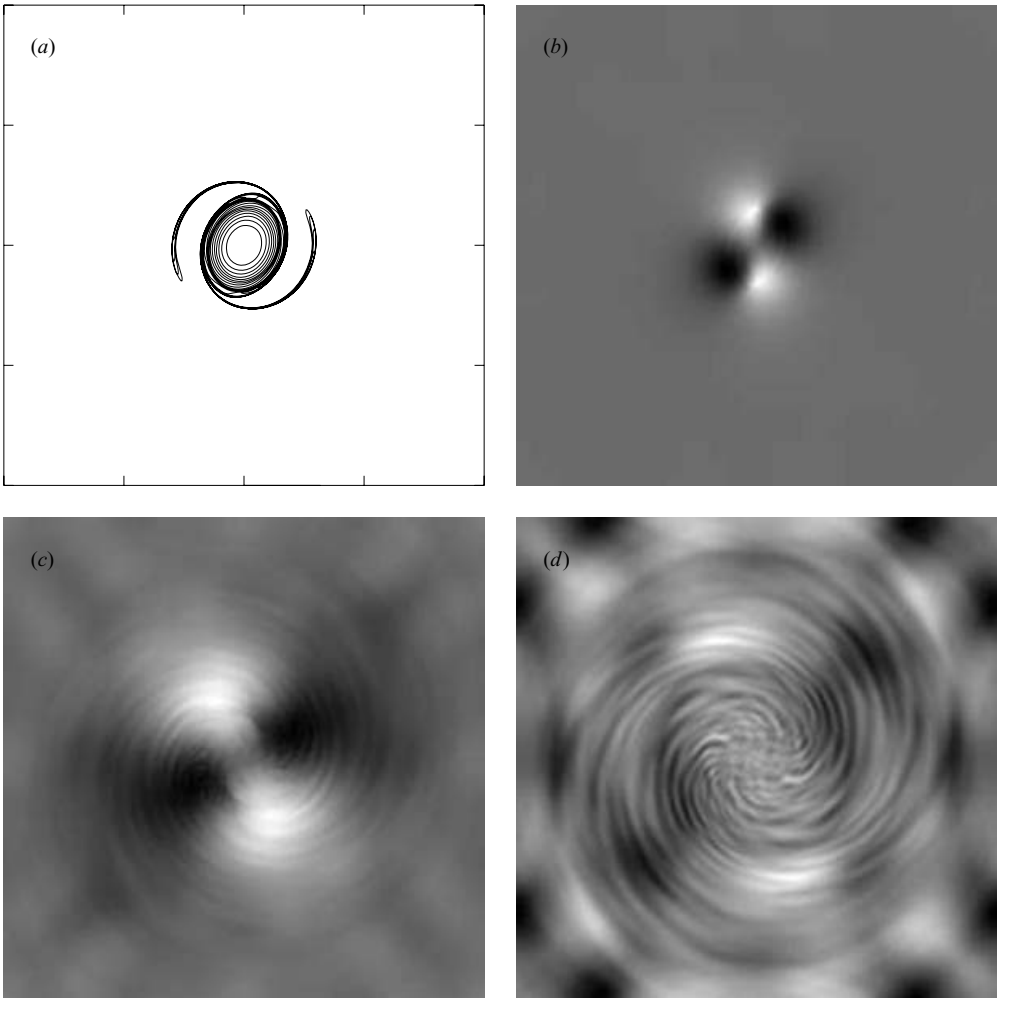

FIGURE 1. Horizontal distributions at $t = 9\,T_{\rm ip}$ of: (*a*) PV jumps at $z = 0$ (jump value $\backsimeq 0.05$), and (*b–d*) vertical velocity w at (*b*) $z = -0.39$ ($\Delta w = [-1.2, 1.7] \times 10^{-3}$), (*c*) $z = -1.18$ ($\Delta w = [-4.5, 6.7] \times 10^{-5}$), and (*d*) $z = -2.15$ ($\Delta w = [-1.2, 1.3] \times 10^{-5}$). The horizontal domain is $\Delta x = \Delta y = [-\pi, \pi]c$.

order 1, i.e. 10^3 times larger that w as is typical of mesoscale oceanic flows (e.g. Pallás-Sanz & Viúdez 2005).

The spiralling of the IGW patterns depends on the phase rotation of the vortical structure. Cyclonic patterns of IGWs can be generated from a single cyclone as long as the vortex departs from sphericity. As a simple example we consider an ellipsoidal cyclone (figure 2*a*) having an initial PV configuration similar to the previous case but with $\varpi_{\max} = 2$ and axes $A_x = 1.6c$, $A_y = 1c$, and $A_z = 1.6$. In this case the flow reaches, between $t = 5T_{\rm ip}$ and $12\,T_{\rm ip}$, extreme values of $\mathscr{R}_{\max} = 0.92$, $\mathscr{F}_{\max} = 0.31$, and $\mathscr{D}_{z\max} = 0.35$, with time-averaged values $\langle \mathscr{R}_{\max} \rangle = 0.92$ (± 0.002), $\langle \mathscr{F}_{\max} \rangle = 0.31$ (± 0.003), and $\langle \mathscr{D}_{z\max} \rangle = 0.35$ (± 0.0002). The characteristics of the IGWs are similar to the previous case. In shallow layers the w displays the mesoscale quadrupolar pattern (figure 2*b*), whereas in mid (figure 2*c*) and deep (figure 2*d*) layers the magnitude of

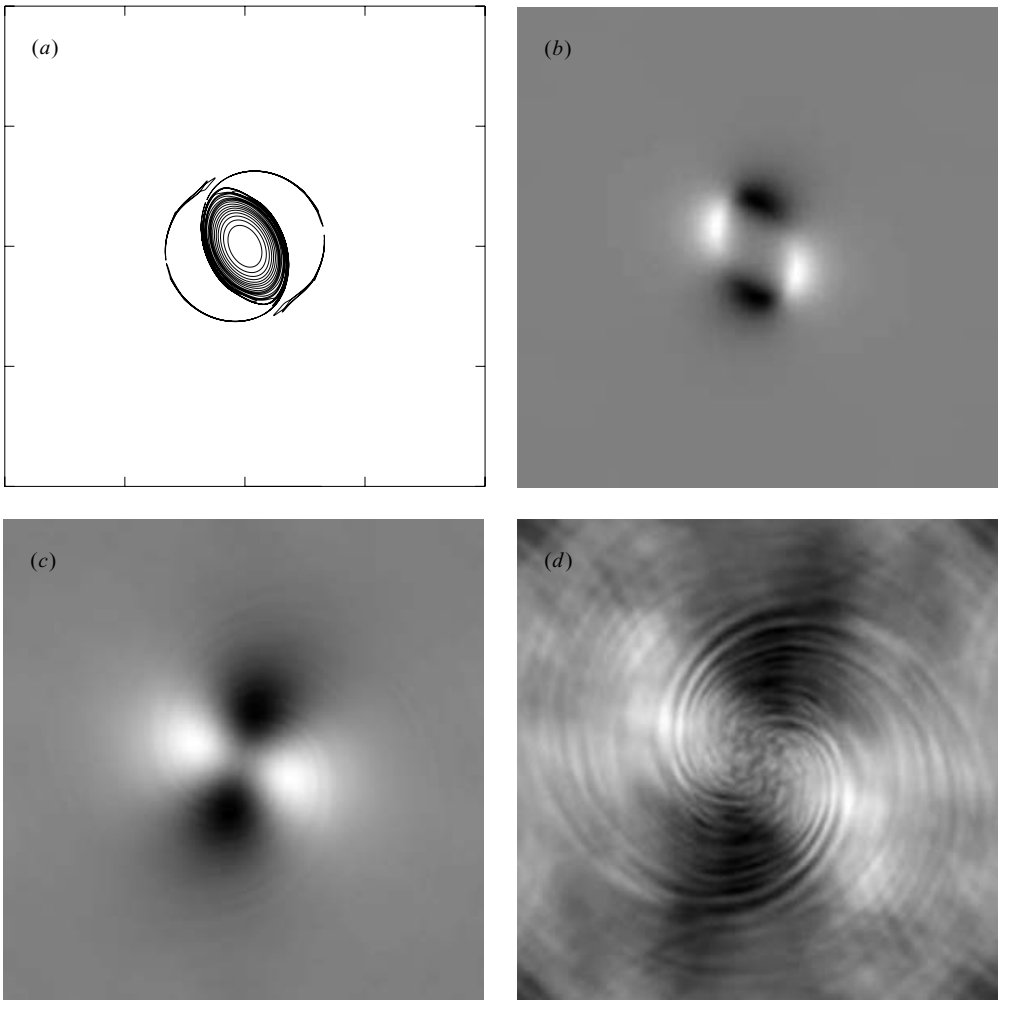

FIGURE 2. As figure 1 but for $\varpi_{\max} = 2$ and $t = 12\,T_{\rm ip}$. The vertical velocity extrema are (*b*) $\Delta w = [-1.8, 1.8] \times 10^{-3}$, (*c*) $\Delta w = [-1.8, 1.8] \times 10^{-4}$, and (*d*) $\Delta w = [-1.7, 1.8] \times 10^{-5}$.

the balanced w decreases and the spiral patterns of IGWs are clearly observed, in this case with cyclonic spiralling.

2.3. *Merging of two vortices*

Enhancement of the IGW generation occurs when the PV advection in the surface layer increases. This in turn implies larger vertical shears and therefore larger Froude numbers. As an example of large-PV advection we consider the merging of two initially spherical (in the quasi-geostrophic space of extent (L_x, L_y, cL_z)) co-rotating vortices. In the case shown in figure 3 ($\varpi_{\min} = -0.95$) the two anticyclones have at $t = 0$ horizontal and vertical radii $r_h = 0.5c$ and $r_z = 0.5$, respectively, with their centres separated by a distance $\delta = 2 \times r_h + 0.02c$. The relevant parameters are given in table 1 for three different numerical experiments with $\varpi_{\min} = -0.75$, -0.85, and -0.95. During the merging process the vortices emit two packets in IGWs, which

$\varpi_{\min}$	$\mathscr{R}_{\min}$	$\mathscr{F}_{\max}$	$\mathscr{D}_{z\max}$	$\langle\mathscr{R}_{\min}\rangle$	$\langle\mathscr{F}_{\max}\rangle$	$\langle\mathscr{D}_{z\max}\rangle$
−0.75	−0.67	0.46	0.46	−0.64 (±0.012)	0.38 (±0.06)	0.37 (±0.05)
−0.85	−0.78	0.62	0.58	−0.76 (±0.009)	0.51 (±0.08)	0.47 (±0.08)
−0.95	−0.93	0.83	0.66	−0.90 (±0.009)	0.68 (±0.10)	0.57 (±0.08)

TABLE 1. Extreme and time-averaged values of $\mathscr{R}$, $\mathscr{F}$, and $\mathscr{D}_z$ for three numerical simulations of two merging anticyclones with different $\varpi_{\min}$. The time average ranges from $t = 5T_{\rm ip}$ to $10\,T_{\rm ip}$ (standard deviations are included).

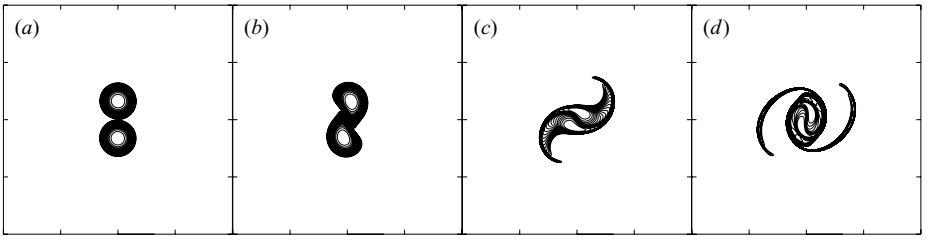

FIGURE 3. (*a–d*) Time sequence of PV contours at $z = 0$ and $t = 1\,T_{\rm ip}$, $3\,T_{\rm ip}$, $6\,T_{\rm ip}$, and $9\,T_{\rm ip}$.

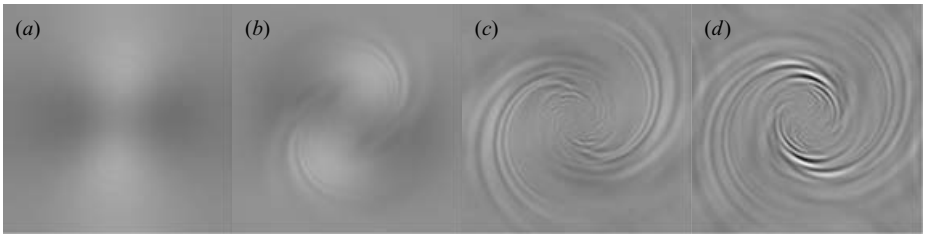

FIGURE 4. w at $z = -2.15$ and (*a*) $t = 5\,T_{\rm ip}$ ($\Delta w = [-2.2, 2.3] \times 10^{-5}$), (*b*) $t = 6\,T_{\rm ip}$ ($\Delta w = [-2.0, 2.6] \times 10^{-5}$), (*c*) $t = 8\,T_{\rm ip}$ ($\Delta w = [-2.6, 2.5] \times 10^{-5}$), and (*d*) $t = 9\,T_{\rm ip}$ ($\Delta w = [-11, 8.9] \times 10^{-5}$) in the case $\varpi_{\min} = -0.95$. The grey scale range is $[-11, 8.9] \times 10^{-5}$.

produce spiral IGW patterns in deep layers (figure 4). During the vortex merging the vortices acquire ellipticity (figure 5*a*), which generates large PV gradients to the rear of the anticyclonically rotating ellipsoid (marked *G* in figure 5*b*). Large negative values of PV advection occur to the rear of each vortex in the resulting anticyclone, where the phase motion is large (the IGW sources marked *S* in figure 5*c*). Two packets of IGWs are generated off the merging anticyclones and propagate downwards and horizontally in the direction of the vortex phase rotation (figures 4*b–d* and 5*d*). Other extrema of PV advection located inside the vortex (marked *s* in figure 5*c*) may generate IGWs but these remain trapped in the anticyclone and do not seem to generate spiral IGW patterns.

The time series of $\mathscr{F}_{\max}$ for the different values of $\varpi_{\min}$ (figure 6*a*) shows the increase of $\mathscr{F}_{\max}$ after the initialization period, reaching maximum values between $t = 7\,T_{\rm ip}$ and $9\,T_{\rm ip}$. The horizontal wavenumber spectra $\hat{W}^2(k_h(k,l), i_z, t) \equiv \sum \hat{w}^2(\pm k, \pm l, i_z, t)$, where $\hat{w}(k, l, i_z, t)$ is the Fourier coefficient of the horizontal wavenumber (k, l) at time t on level i_z, and $k_h^2(k,l) \equiv k^2 + l^2$ is the squared horizontal wavenumber, is shown in figure 6(*b*,*c*,*d*) for different values of $\varpi_{\min}$. The amplitude of small scales (IGWs) clearly increases with time in mid and deep layers for the three values of

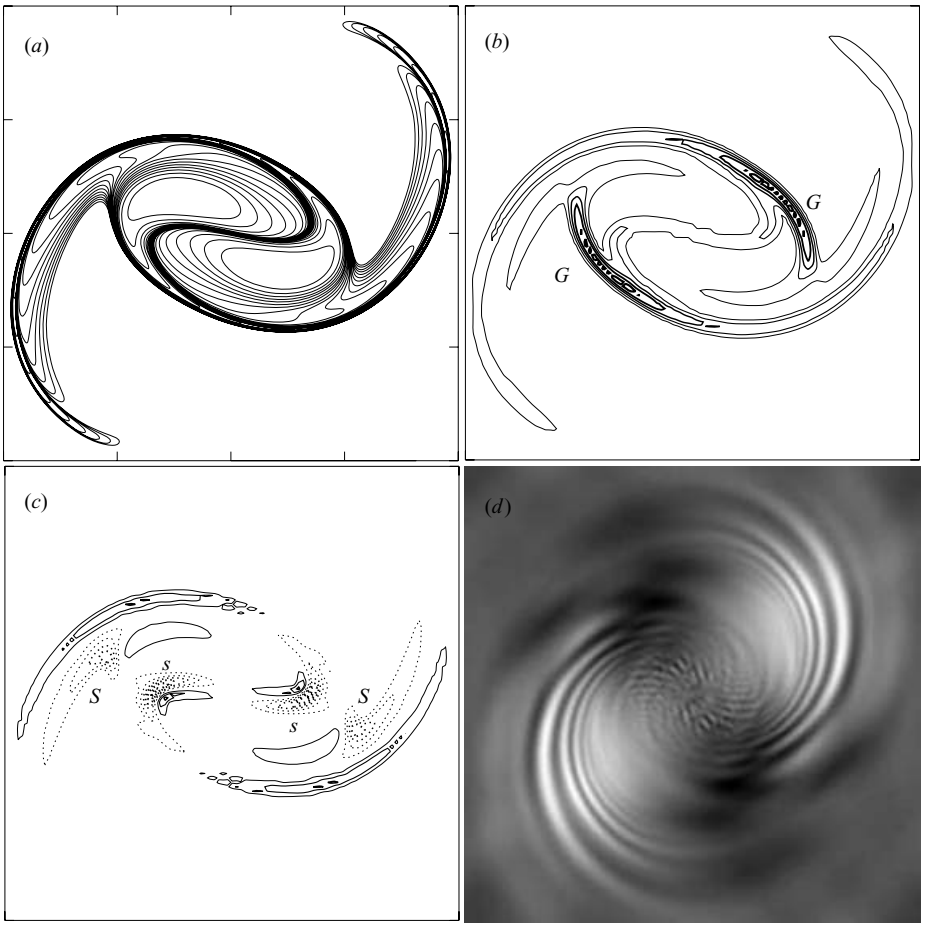

FIGURE 5. A closer view at $z=0$ and $t=7\,T_{\rm ip}$ of (a) the PV contours, (b) the horizontal distribution of $|\nabla_h\varpi|$ ($|\nabla_h\varpi|_{\max}=2.2$, contour interval $\delta=0.2$, zero contour omitted), and (c) the horizontal distribution of the horizontal PV advection $\boldsymbol{u}_h\cdot\nabla_h\varpi$ ($\Delta=\{-0.62, 0.47\}$, contour interval $\delta=0.05$, zero contour omitted). (d) Horizontal distribution (entire domain) of w at $z=-2.15$ and $t=7\,T_{\rm ip}$ ($\Delta w=[-1.8, 2.9]\times10^{-5}$).

$\varpi_{\min}$. In shallower layers the large scale w evolves in the opposite direction, towards larger scales, which is probably due to the fact that the mesoscale w evolves, during the merging process, from the small scales of the two initial anticyclones to the large scale of the merged vortex.

2.4. *Dipole*

The dipolar vortex is an example of a vortical structure where, despite the fact that vortex phase rotations are largely inhibited, spiral patterns of IGWs are also generated. The dipole is here simulated as anticyclone ($-$) and cyclone ($+$) PV ellipsoids with extreme $\varpi^{\pm}=\pm0.95$ and axes $A_x^{\pm}=1.2c$, $A_y^{\pm}=1c$, $A_z^{\pm}=\{1, 0.6\}$ in the initial configuration. The flow reaches extreme values $\mathscr{R}_{\min}=-0.92$, $\mathscr{R}_{\max}=0.53$, $\mathscr{F}_{\max}=0.56$, and $\mathscr{D}_{z\max}=0.44$, with averaged values, from $t=5\,T_{\rm ip}$ to $14\,T_{\rm ip}$, $\langle\mathscr{R}_{\min}\rangle=-0.92$ (±0.0006), $\langle\mathscr{R}_{\max}\rangle=0.52$ (±0.009), $\langle\mathscr{F}_{\max}\rangle=0.53$ (±0.01), and $\langle\mathscr{D}_{z\max}\rangle=0.44$ (±0.001).

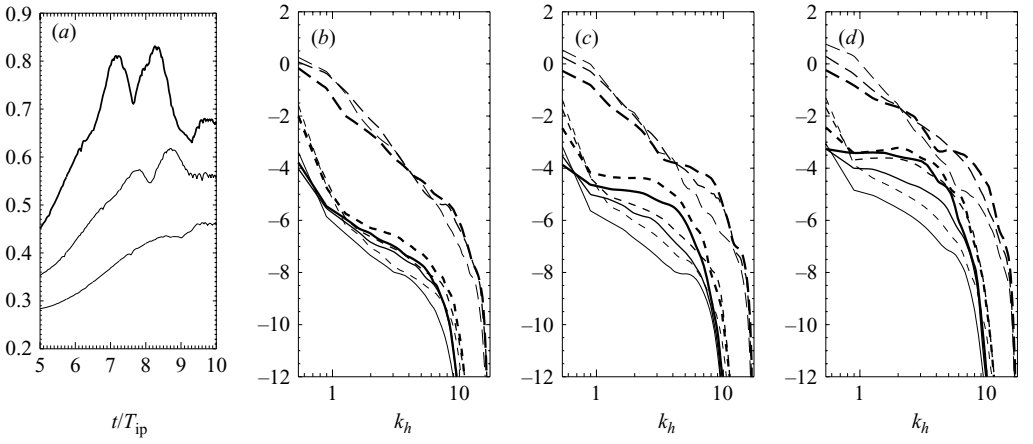

FIGURE 6. (*a*) Time series of $\mathscr{F}_{\max}$ for $\varpi_{\min} = -0.75$ (thin line), -0.85 (medium thick line), and -0.95 (thick line). (*b–d*) Horizontal wavenumber spectra $\log \hat{W}^2(k_h)$ on the planes $i_z = 41$ ($z = -2.15$, solid lines), $i_z = 81$ ($z = -1.18$, dotted lines), and $i_z = 121$ ($z = -0.2$, dashed lines), and times $t = 6$ (thin lines), 8 (medium thick lines), and $10\,T_{\rm ip}$ (thick lines), for $\varpi_{\min} = -0.75$ (*b*), -0.85 (*c*), and -0.95 (*d*).

As the dipole propagates eastward (figure 7*a*) the mesoscale w in the shallow layers displays the large-scale quadrupole pattern (figure 7*c*) typical of the quasi-geostrophic balance. Anticyclonic patterns of IGWs due to the anticyclone appear clearly in deep layers (figure 7*d*).

Besides the spiral IGWs, a frontal wave packet ahead of the dipole, noticeable in the horizontal distribution of w in shallow and mid layers (marked with an arrow in figure 7*b*, *c*) is generated. This frontal wave is steady in the reference frame of the propagating dipole and seems to be a consequence of the large velocity of propagation (westward) of the dipole being opposite to the horizontal group velocity (otherwise eastward) of the frontal wave packet. This wave packet, though also spontaneously generated by the dipole, seems to be different from the spiral IGW patterns and its characteristics will be addressed elsewhere.

The generation of the spiral patterns of IGWs by the dipole seems to be related to the small phase oscillations experienced in this case by the anticyclone. The largest values of PV advection ($\boldsymbol{u}\cdot\nabla\varpi = -\partial\varpi/\partial t$) in the dipole are related to these small perturbations (figure 8) rather than to the speed of displacement of the dipole as a whole. These small perturbations have the same sign of rotation as the vortex to which they belong. In this case, these perturbations are faster in the anticyclone, whose magnitude of relative vorticity is larger than in the cyclone. This explains the generation of the spiral patterns of IGWs predominantly by the anticyone.

2.5. *Anticyclonic baroclinic instability*

The spontaneous generation of IGW packets by balanced flow and the development of spiral wave patterns also occur in flows more complex than the above simple cases. We consider, as the last example, the baroclinic instability of an anticyclonic shear flow, here simulated using an initially perturbed PV cylinder of horizontal and vertical radii $r_h = 0.5c$ and $r_z = \sqrt{2}$, respectively, and minimum $\varpi_{\min} = -0.75$ (details on the PV cylinder configuration are given in Dritschel & Viúdez 2003). The PV rolls up into a street of anticyclones (figure 9), at $t = 7\,T_{\rm ip}$ reaching $\mathscr{R}_{\min} = -0.68$ and $\mathscr{F}_{\max} = 0.35$. The balanced component of the flow ($\boldsymbol{u}_{\rm b}$) is obtained diagnostically

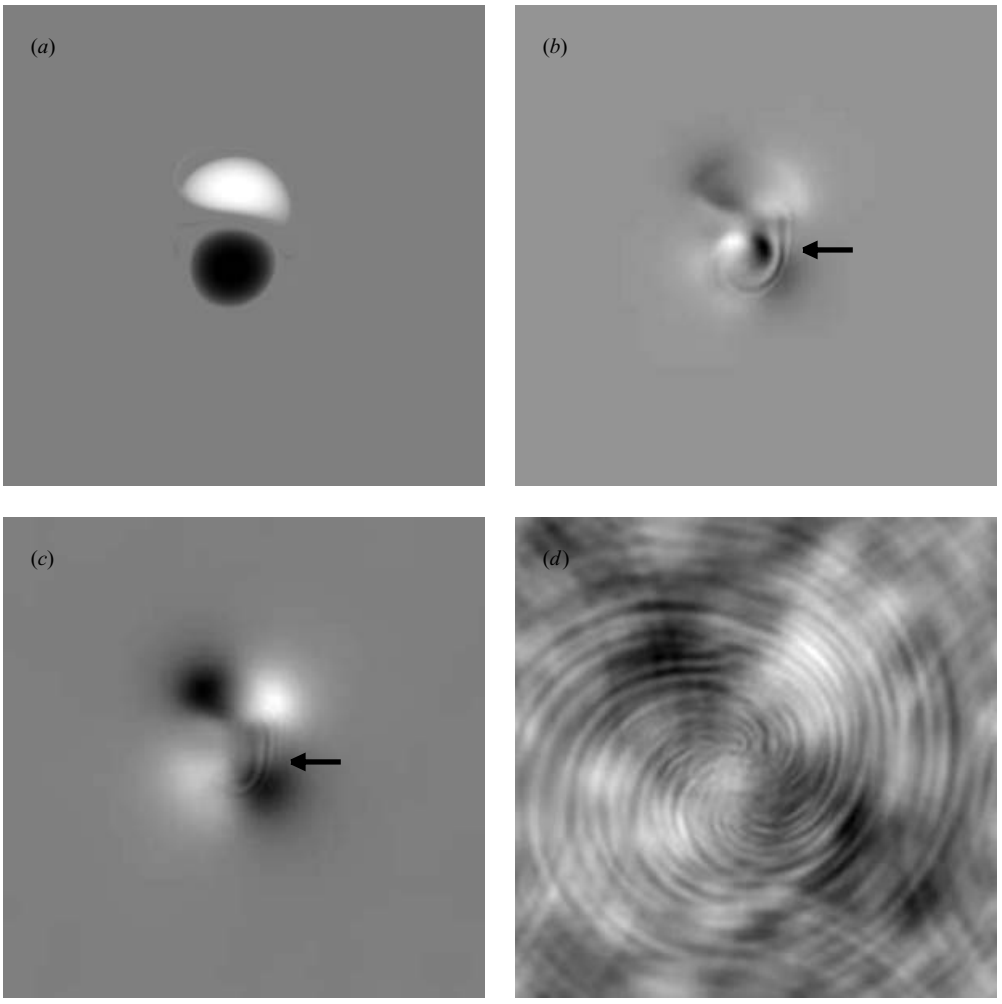

FIGURE 7. Horizontal distributions at $t = 14\,T_{\rm ip}$ of (a) ϖ at $z = 0$ $(\Delta\varpi = [-0.95, 0.95])$, and $(b$–$d)$ w at (b) $z = -0.20$ $(\Delta w = [-2.1, 1.5] \times 10^{-3})$, (c) $z = -0.39$ $(\Delta w = [-8.3, 8.6] \times 10^{-4})$, and (d) $z = -2.15$ $(\Delta w = [-1.5, 1.5] \times 10^{-5})$.

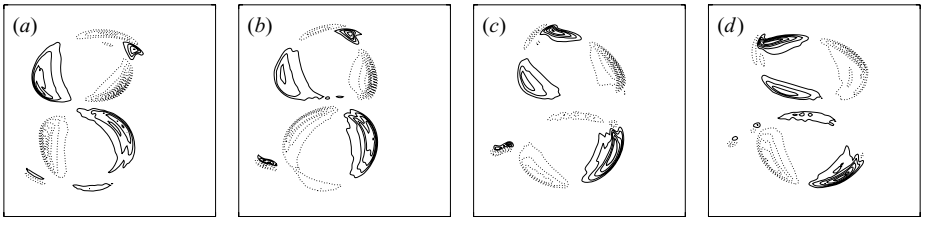

FIGURE 8. $(a$–$d)$ Time series from $t = 10\,T_{\rm ip}$ to $13\,T_{\rm ip}$ of $\boldsymbol{u} \cdot \nabla\varpi$ at $z = 0$ (contour interval $\delta = 0.01$, zero contour omitted).

(in this case in a 128^3 grid-point simulation) from the PV field using the optimal PV balance approach (Viúdez & Dritschel 2004). The unbalanced component of the flow (the IGWs) is obtained from the total ($\boldsymbol{u}$) and balanced flows as the difference

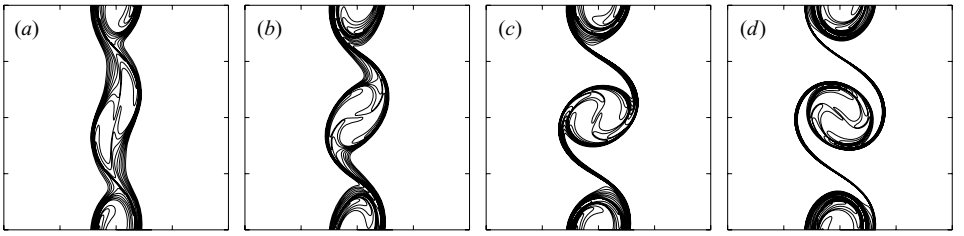

FIGURE 9. (a–d) Time series from $t = 5\,T_{\rm ip}$ to $8\,T_{\rm ip}$ of the PV jumps at $z = 0$ in the anticyclonic shear instability case (jump value $\backsimeq 0.04$).

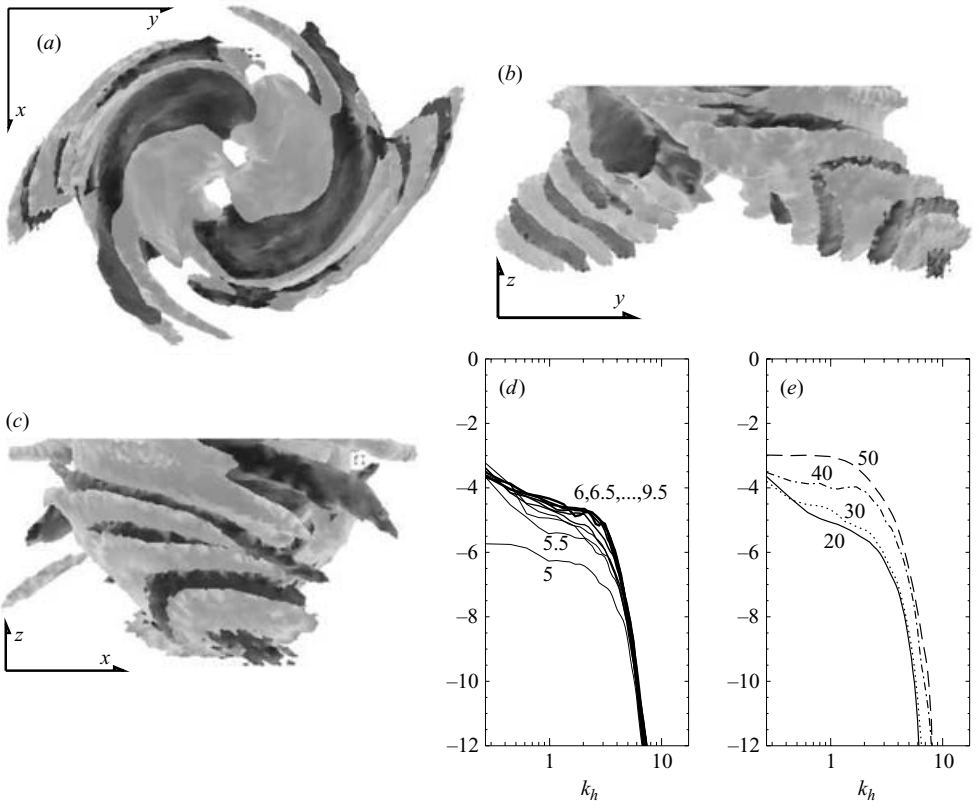

FIGURE 10. (a–c) Isosurfaces of the unbalanced vertical velocity $w_{\rm i} = \pm 5 \times 10^{-5}$ at $t = 7.3\,T_{\rm ip}$ in the anticyclone viewed from (a) the top, (b) east, and (c) south. (d, e) Wavenumber spectra of $w_{\rm i}$, $\log \hat{W}_{\rm i}^2(k_h)$, ($d$) at $z = -1.57$ and at different times (in $T_{\rm ip}$), and (e) at $t = 7.3\,T_{\rm ip}$ on planes $i_z = \{20, 30, 40, 50\}$ ($z = \{-2.21, -1.72, -1.28, -0.74\}$).

$\boldsymbol{u}_{\rm i} \equiv \boldsymbol{u} - \boldsymbol{u}_{\rm b}$. The isosurfaces of the unbalanced component of the vertical velocity $w_{\rm i}$ (figure 10a, b, c) show that two packets of IGWs are generated at $z = 0$ in the anticyclone (the vortex having larger ellipticity and larger PV advection located in the centre of the domain) and propagate downwards forming a pattern of spiral waves. The wavenumber spectra of $w_{\rm i}$ as a function of time at a given depth (figure 10d) show the increase of IGW amplitude with time until wave saturation occurs at $t \simeq 8\,T_{\rm ip}$, as well as the decrease of wave amplitude with depth (figure 10e).

3. Concluding remarks

We have seen simple examples of initially balanced geophysical flows that, remaining static and inertially stable and owing to the spontaneous emission of IGW packets, eventually display spiral patterns of waves. The spiral wave patterns may be qualitatively explaining by noticing that, first, the time-dependent vortical flow emits discrete packets of IGWs in regions of large PV advection (the IGW sources), or equivalently since PV is conserved, in regions of large local rate of change of PV. The wave packets generated inside the vortices remain trapped while the ones generated along the boundaries of the vortical flow propagate downwards (and upwards), leave the vortical flow, and disperse. The initial propagation of these IGWs, still in the vortical flow, is faster along isopycnals, which makes the surfaces of equal phase acquire curvature because of the curvature of the vortical flow itself (i.e. the curved isopycnals in the vortices partially guide the waves while these remain in the vortical flow). Onto this IGW emission another effect is superimposed: the fact that the IGW packets are emitted during a finite period of time from the moving sources. This horizontal displacement of the IGW sources causes the spiraling of the wave patterns. Thus, anticyclonic (cyclonic) moving sources give rise to anticyclonic (cyclonic) spiral wave patterns.

The spiral waves are initially noticeable in the vertical velocity in deep layers, where their vertical velocity is larger than the vertical velocity of the balanced flow, but they occur everywhere in the fluid column. Spiral wave patterns seem to be, therefore, a robust property, rather than an exception, of time-dependent mesoscale baroclinic geophysical flows. Their importance in the transition to geostrophic turbulence remains unexplored.

I thank the Barcelona Supercomputing Center (www.bsc.es) for their help in the use of the parallel computer *MareNostrum*, and the comments from three anonymous reviewers.

REFERENCES

Barnes, D. R. & Kerswell, R. R. 2000 New results in rotating Hagen-Poiseuille flow. *J. Fluid Mech.* **417**, 103–126.

Dritschel, D. G. & Viúdez, A. 2003 A balanced approach to modelling rotating stably-stratified geophysical flows. *J. Fluid Mech.* **488**, 123–150.

Molemaker, M. J., McWilliams, J. C. & Yavneh, I. 2005 Baroclinic instability and loss of balance. *J. Phys. Oceanogr.* **35**, 1505–1517.

Smith, F. T. & Bodonyi, R. J. 1982 Amplitude-dependent neutral-modes in the Hagen-Poiseuille flow through a circular pipe. *Proc. R. Soc. Lond.* A 384, 463–489.

Pallàs-Sanz, E. & Viúdez, A. 2005 Diagnosing mesoscale vertical velocity from horizontal velocity and density data. *J. Phys. Oceanogr.* **35**, 1744–1762.

Toplosky, N. & Akylas, T. R. 1988 Nonlinear spiral waves in rotating pipe flow. *J. Fluid Mech.* **190**, 39–54.

Viúdez, A. & Dritschel, D. G. 2003 Vertical velocity in mesoscale geophysical flows. *J. Fluid Mech.* **483**, 199–223.

Viúdez, A. & Dritschel, D. G. 2004 Optimal potential vorticity balance of geophysical flows. *J. Fluid Mech.* **521**, 343–352.

Viúdez, A. & Dritschel, D. G. 2006 Spontaneous generation of inertia-gravity wave packets by balanced geophysical flows. *J. Fluid Mech.* **553**, 107–117.

Wedin, H. & Kerswell, R. R. 2004 Exact coherent structures in pipe flow: travelling wave solutions. *J. Fluid Mech.* **508**, 333–371.